

Measurement of the beam-helicity asymmetry I^\odot in the photoproduction of $\pi^0\pi^\pm$ -pairs off protons and off neutrons

M. Oberle¹, J. Ahrens², J.R.M. Annand³, H.J. Arends², K. Bantawa⁴, P.A. Bartolome², R. Beck⁵, V. Bekrenev⁶, H. Berghäuser⁷, A. Braghieri⁸, D. Branford⁹, W.J. Briscoe¹⁰, J. Brudvik¹¹, S. Cherepnya¹², B. Demissie¹⁰, M. Dieterle¹, E.J. Downie^{2,3,10}, P. Drexler⁷, L.V. Fil'kov¹², A. Fix¹³, D.I. Glazier⁹, E. Heid², D. Hornidge¹⁴, D. Howdle³, G.M. Huber¹⁵, O. Jahn², I. Jaegle¹, T.C. Jude⁹, A. Käser¹, V.L. Kashevarov^{12,2}, I. Keshelashvili¹, R. Kondratiev¹⁶, M. Korolija¹⁷, S.P. Kruglov⁶, B. Krusche¹, A. Kulbardi⁶, V. Lisin¹⁶, K. Livingston³, I.J.D. MacGregor³, Y. Maghrbi¹, J. Mancell³, D.M. Manley⁴, Z. Marinides¹⁰, M. Martinez², J.C. McGeorge³, E. McNicoll³, D. Mekterovic¹⁷, V. Metag⁷, S. Micanovic¹⁷, D.G. Middleton¹⁴, A. Mushkarenkov⁸, B.M.K. Nefkens¹¹, A. Nikolaev⁵, R. Novotny⁷, M. Ostrick², B. Oussena^{2,10}, P. Pedroni⁸, F. Pheron¹, A. Polonski¹⁶, S.N. Prakhov¹¹, J. Robinson³, G. Rosner³, T. Rostomyan^{1,8}, S. Schumann², M.H. Sikora⁹, D.I. Sober¹⁸, A. Starostin¹¹, I. Supek¹⁷, M. Thiel⁷, A. Thomas², M. Unverzagt^{2,5}, D.P. Watts⁹, D. Werthmüller¹, L. Witthauer¹, F. Zehr¹
(The Crystal Ball at MAMI, TAPS, and A2 Collaborations)

¹ Department of Physics, University of Basel, CH-4056 Basel, Switzerland

² Institut für Kernphysik, University of Mainz, D-55099 Mainz, Germany

³ School of Physics and Astronomy, University of Glasgow, G12 8QQ, United Kingdom

⁴ Kent State University, Kent, Ohio 44242, USA

⁵ Helmholtz-Institut für Strahlen- und Kernphysik, University of Bonn, D-53115 Bonn, Germany

⁶ Petersburg Nuclear Physics Institute, RU-188300 Gatchina, Russia

⁷ II. Physikalisches Institut, University of Giessen, D-35392 Giessen, Germany

⁸ INFN Sezione di Pavia, I-27100 Pavia, Pavia, Italy

⁹ School of Physics, University of Edinburgh, Edinburgh EH9 3JZ, United Kingdom

¹⁰ Center for Nuclear Studies, The George Washington University, Washington, DC 20052, USA

¹¹ University of California Los Angeles, Los Angeles, California 90095-1547, USA

¹² Lebedev Physical Institute, RU-119991 Moscow, Russia

¹³ Laboratory of Mathematical Physics, Tomsk Polytechnic University, Tomsk, Russia

¹⁴ Mount Allison University, Sackville, New Brunswick E4L1E6, Canada

¹⁵ University of Regina, Regina, SK S4S-0A2 Canada

¹⁶ Institute for Nuclear Research, RU-125047 Moscow, Russia

¹⁷ Rudjer Boskovic Institute, HR-10000 Zagreb, Croatia

¹⁸ The Catholic University of America, Washington, DC 20064, USA

the date of receipt and acceptance should be inserted later

Abstract. Beam-helicity asymmetries have been measured at the MAMI accelerator in Mainz for the photoproduction of mixed-charge pion pairs in the reactions $\gamma p \rightarrow n\pi^0\pi^+$ off free protons and $\gamma d \rightarrow (p)p\pi^0\pi^-$ and $\gamma d \rightarrow (n)n\pi^0\pi^+$ off quasi-free nucleons bound in the deuteron for incident photon energies up to 1.4 GeV. Circularly polarized photons were produced from bremsstrahlung of longitudinally polarized electrons and tagged with the Glasgow-Mainz magnetic spectrometer. The charged pions, recoil protons, recoil neutrons, and decay photons from π^0 mesons were detected in the 4π electromagnetic calorimeter composed of the Crystal Ball and TAPS detectors. Using a complete kinematic reconstruction of the final state, excellent agreement was found between the results for free and quasi-free protons, suggesting that the quasi-free neutron results are also a close approximation of the free-neutron asymmetries. A comparison of the results to the predictions of the Two-Pion-MAID reaction model shows that the reaction mechanisms are still not well understood, in particular at low incident photon energies in the second nucleon-resonance region.

PACS. 13.60.Le Meson production – 14.20.Gk Baryon resonances with S=0 – 25.20.Lj Photoproduction reactions

1 Introduction

The excitation spectrum of nucleons is a much discussed topic because it is closely related to the fundamental properties of the strong interaction in the non-perturbative range. The apparently unsatisfactory match [1] between model predictions based on Quantum Chromodynamics ‘inspired’ quark models and the experimental database for excited nucleon states has motivated many recent efforts in experiment and also in theory development. Recent progress for the latter came mostly from the application of the Dyson-Schwinger equation to the QCD Lagrangian (see e.g. [2,3,4]) and from the advances in lattice gauge calculations and their combination with the methods of chiral perturbation theory for the extrapolation to physical quark masses. First unquenched lattice results, which recently became available [5], basically ‘re-discovered’ the $SU(6)\otimes O(3)$ excitation structure of the nucleon with a level counting consistent with the standard non-relativistic quark model. However, one should keep in mind that these calculations are still at a very early stage. On the experimental side, over the last decade, much effort has been made to overcome the limitations in the available database, which was dominated by the results from pion scattering on nucleons and thus biased against nucleon resonances with small couplings to $N\pi$. Due to the advances in accelerator and detector technology, photoproduction of mesons has become a prime tool in this research.

It was soon realized that sequential decays involving intermediate excited states play an essential role, especially for higher lying resonances. This is in analogy to nuclear physics, where a restriction to the ground-state decays of excited states would have resulted in a very limited picture of nuclear structure, missing fundamentally important features like collective rotational or vibrational bands. Since excited nucleon states decay almost exclusively via meson emission, the only possibility is to study reactions with meson multiplicity larger than one in the final state. Therefore, such reactions have attracted much interest in recent years. In particular, the production of pseudoscalar meson pairs, mostly pion pairs but also pion eta pairs, has been experimentally studied. Special attention was paid to neutral mesons ($\pi^0\pi^0$ and $\pi^0\eta$, see [6, 7, 8, 9, 10, 11, 12, 13, 14, 15, 16, 17, 18, 19, 20, 21] for recent results). The reason is that non-resonant background terms are more important for charged pions since the incident photon can couple directly to them.

However, the measurement of different charge combinations of the pion pairs and also measurements of their production off both protons and neutrons is mandatory for an isospin decomposition of the reaction, helping to identify contributions from N^* and Δ^* resonances. Furthermore, reactions with at least one charged pion in the final state should allow the investigation of contributions from resonance decays by emission of the ρ meson. The

ρ^\pm meson decays to $\pi^0\pi^\pm$ pairs while the ρ^0 meson cannot decay to $\pi^0\pi^0$ pairs but only to $\pi^+\pi^-$ pairs.

Predictions for many different observables for all possible isospin channels are available from the Two-Pion-MAID reaction model by Fix and Arenhövel [22]. The model is based on an effective Lagrangian approach with Born and resonance diagrams at the tree level. They are summarized in Fig. 1. The most interesting diagrams for the investigation of nucleon resonances are 3(a) and 3(b) which include all s -channel Breit-Wigner resonances R with $J \leq 5/2$ for which all parameters like $N\gamma$ coupling and partial $R \rightarrow \pi\Delta$ and $R \rightarrow N\rho$ decay widths were taken from the Particle Data Group. Diagram 3(a) corresponds to sequential resonance decays where a higher lying excited state (N^* or Δ^*) decays to the $\Delta(1232)$ resonance. Diagram 3(b) corresponds to the direct groundstate $N\rho$ -decays of nucleon resonances. Non-resonant background contributions arise from the nucleon-nucleon and nucleon- Δ Born-terms and from pion-pole terms. Non-resonant background contributes also for the charged ρ -meson for example from the ρ -Kroll-Ruderman term (diagram 1(h)) and the pion-pole term (1(i)). The contributions of the non-resonant backgrounds for charged mesons may be substantial. This is already reflected [1] in the absolute magnitude ($\sigma \approx 10 \mu\text{b}$ for $\pi^0\pi^0$, $\sigma \approx 50 \mu\text{b}$ for $\pi^0\pi^+$, $\sigma \approx 75 \mu\text{b}$ for $\pi^+\pi^-$) of the total cross section for the different charge states at the second nucleon resonance region composed of the $P_{11}(1440)$, $D_{13}(1520)$, and $S_{11}(1535)$ state.

Production of $\pi^+\pi^-$ pairs has been studied by electron scattering at the CLAS facility at JLab [23,24]. The results have been interpreted in the framework of a phenomenological meson-baryon reaction model and used to extract electrocouplings for the $P_{11}(1440)$ and $D_{13}(1525)$ resonances [25,26].

The first precise measurements of the total cross section and the invariant-mass distributions of pion-pion and pion-nucleon pairs for the $\pi^0\pi^+$ final state for photoproduction off the proton in the second resonance region was done with the DAPHNE [27] and TAPS [28] experiments at the MAMI accelerator in Mainz. They revealed strong discrepancies with all available model predictions [1, 28]. It was then suggested that the main effect was caused by the neglect of ρ contributions in the models (due to the relatively large mass of this meson, ρ contributions had been neglected in the second resonance region.) Including such terms significantly improved the agreement between reaction models and experimental results [29,30]. Particularly, the invariant-mass distributions measured by DAPHNE for $\gamma n \rightarrow p\pi^-\pi^0$ [8] in quasi-free kinematics off neutrons bound in the deuteron and by TAPS for $\gamma p \rightarrow n\pi^0\pi^+$ [28] supported this interpretation. The latter results were taken as evidence for a significant contribution from the $D_{13}(1520) \rightarrow N\rho$ decay to the photoproduction of mixed charge pairs [28], which was subsequently also confirmed for the $\pi^+\pi^-$ final state in electroproduction [26].

The discussions of the ρ -meson contribution were based on the shape difference of the pion-pion invariant mass distributions for the $\pi^0\pi^0$ and $\pi^0\pi^\pm$ final states and the comparison to the results from reaction models, in particular

Correspondence to: B. Krusche, Klingelbergstrasse 82, CH-4056 Basel, Switzerland, e-mail: Bernd.Krusche@unibas.ch

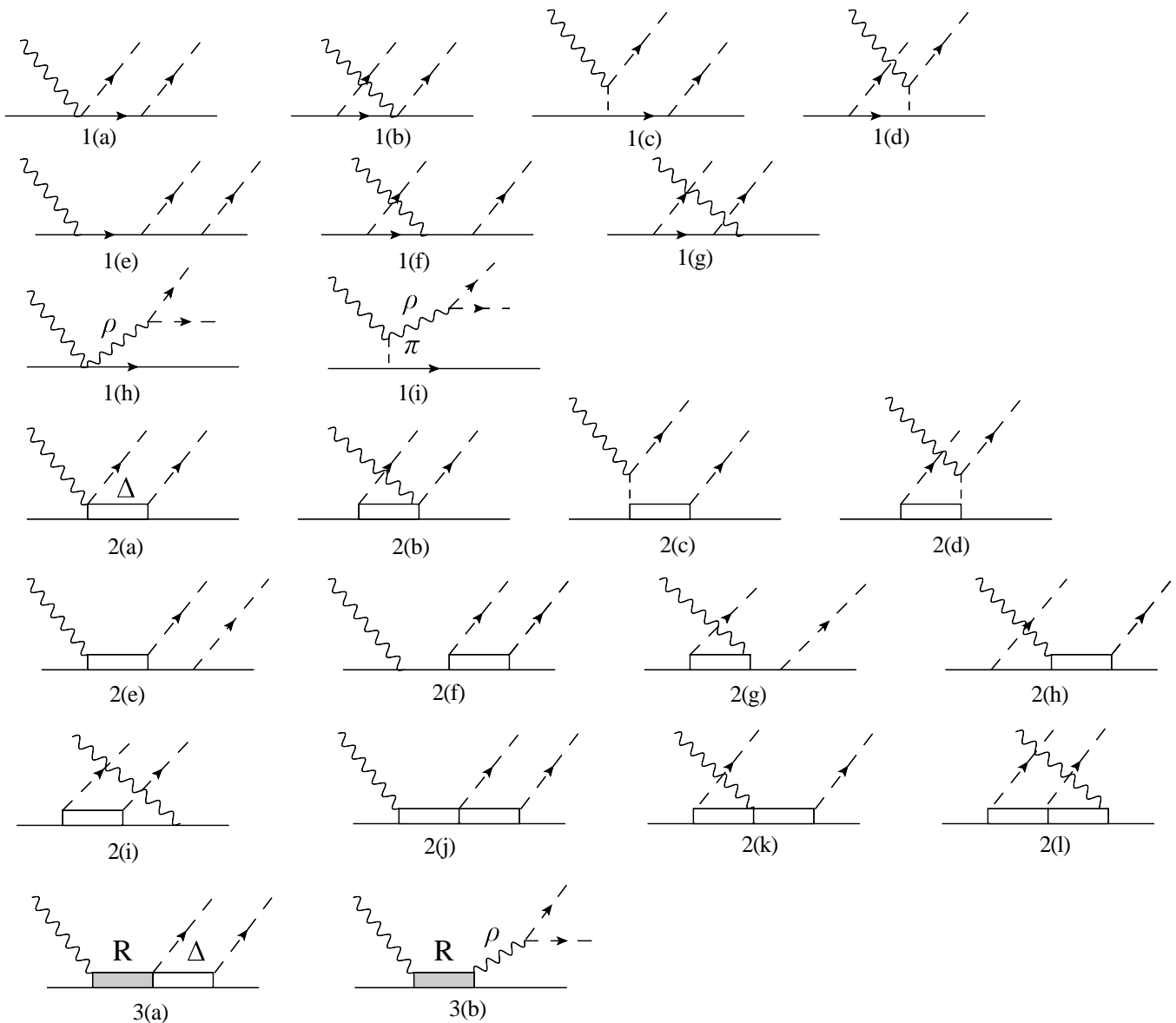


Fig. 1. Contributions to photoproduction of meson pairs at low incident photon energy. Shown are the diagrams that are considered in the Two-Pion-MAID model [22]. Diagrams 1(a) - 1(i) correspond to nucleon Born, pion-pole (c-d,i), and ρ -Kroll Ruderman (h) background terms. Diagrams 2(a) - 2(l) represent similar background terms involving the $\Delta(1232)$ state. The s-channel diagram 3(a) represents sequential decays of higher lying resonances via the $\Delta(1232)$ intermediate state and 3(b) the direct decay of resonances to the nucleon ground state via emission of ρ -mesons.

to the Valencia model [30]. However, the problem is much more complicated. Photoproduction of pseudo-scalar meson pairs off nucleons involves eight complex amplitudes [31] as function of five kinematic variables (for example two Lorentz invariants and three angles). The measurement of eight independent observables would be needed just to extract the magnitude of all amplitudes in a unique way (not even considering ambiguities arising from finite statistical precision of the data). Fixing in addition the phases would require the measurement of 15 observables. It is thus evident that the analysis of differential cross section data alone cannot solve the problem. Analyses based on such a limited data set will always strongly depend on

the model assumptions. A more profound analysis requires the measurement of further observables, exploring polarization degrees of freedom. A fully complete measurement appears unrealistic due to the huge effort needed, but already the measurement of at least some polarization observables can provide valuable constraints for the reaction models.

The reaction $\gamma p \rightarrow n\pi^0\pi^+$ has been measured with the DAPHNE detector at MAMI with a circularly polarized photon beam and a longitudinally polarized target for incident photon energies up to 800 MeV [32]. The results have been used to split the cross section into the $\sigma_{3/2}$ (photon and proton spins parallel) and $\sigma_{1/2}$ (spins antipar-

allel) components. The result shows a dominance of the $\sigma_{3/2}$ part in the second resonance region. This would be in line with contributions from the $D_{13}(1520)$ resonance, either via the sequential $D_{13} \rightarrow \Delta(1232)\pi \rightarrow N\pi\pi$ decay chain and/or the direct $D_{13} \rightarrow N\rho$ decay. The Valencia model with the ρ -terms and an additional contribution from the $D_{33}(1700)$ resonance [30,33] agreed well with the $\sigma_{3/2}$ component, but somewhat underestimated $\sigma_{1/2}$.

At this point another polarization observable moved into the focus, namely the beam helicity asymmetry I^\odot , measured with circularly polarized photon beams and unpolarized targets. Reaction models [36] had predicted a large sensitivity to small contributions via interference terms. The first measurement of this observable for the $p\pi^+\pi^-$ final state at JLab [34] revealed severe deficiencies in all reaction models for this observable. A subsequent measurement [35] of it for all possible final states off the proton target ($p\pi^+\pi^-$, $n\pi^+\pi^0$, $p\pi^0\pi^0$) in the second resonance region confirmed the results for the doubly charged pion pairs, and showed similar or even worse problems for the mixed-charge final state, while only the measured asymmetries for the $2\pi^0$ final state were reasonably well reproduced by some reaction models. In the meantime, asymmetries for double π^0 production have been measured off free protons and quasi-free protons and neutrons bound in the deuteron up to incident photon energies of 1.4 GeV [15]. Reaction-model results are in reasonable agreement with the measured asymmetries for the reaction off the proton, but less so for the neutron target. A surprising result was that the Valencia model [30,33,36] failed for I^\odot in all isospin channels, although it had reasonably well reproduced all other observables measured so far for the different final states (total cross sections, invariant-mass distributions, $\sigma_{3/2} - \sigma_{1/2}$ decomposition of the cross sections).

The present work reports the results from the measurement of beam-helicity asymmetries in photoproduction of $\pi^0\pi^\pm$ pairs off free protons, quasi-free protons, and neutrons for incident photon energies up to 1.4 GeV. Measurements off the neutron can only be done in quasi-free kinematics off neutrons bound in light nuclei, specifically the deuteron. This is complicated by the nuclear Fermi motion and possible final-state interaction (FSI) effects, but much progress has recently been made in the analysis and interpretation of such reactions [37].

2 Beam-helicity asymmetries

Beam-helicity asymmetries I^\odot can be measured for three-body final states like $N\pi\pi$ with circularly polarized photons and unpolarized targets. This observable is defined by:

$$I^\odot(\Phi) = \frac{d\sigma^+ - d\sigma^-}{d\sigma^+ + d\sigma^-} = \frac{1}{P_\gamma} \frac{N^+ - N^-}{N^+ + N^-}, \quad (1)$$

where $d\sigma^\pm$ are the differential cross sections for each of the two photon helicity states, and P_γ is the degree of circular polarization of the photons. The angle Φ can be defined in different ways in the cm system of the incident

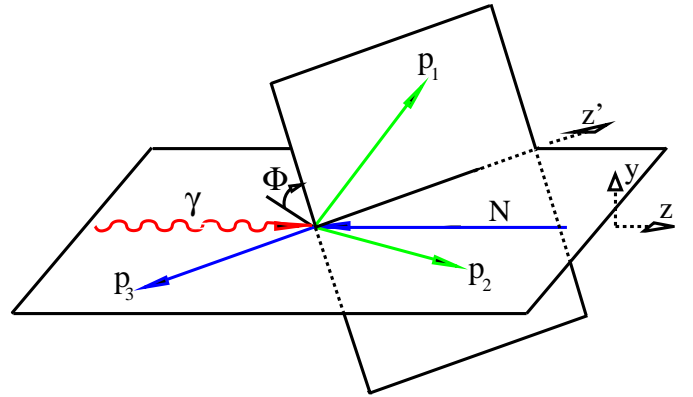


Fig. 2. Vector and angle definitions in the cm system of incident photon (γ) and initial-state participant nucleon N . Particles p_1 , p_2 , and p_3 are some permutation of the final-state participant nucleon N' and the two pions (π^0 , π^\pm), depending on the type of the asymmetry (see text). One plane is defined by the momentum of the incident photon \mathbf{k} and the momentum of particle p_3 , the other by the momenta of particles p_1 and p_2 (all momenta in the photon-nucleon cm system). Φ is the angle between the planes. For the choice $p_3 = N'$, $p_1 = \pi^\pm$, $p_2 = \pi^0$ the planes are the usual reaction and production planes as defined in Refs. [35,36].

photon and the initial state nucleon. This is illustrated in Fig. 2. Two planes are spanned by the incident photon, the recoil nucleon, and the two pions and Φ is the angle between them.

Beam helicity asymmetries are particularly robust with respect to false asymmetries introduced by the experimental setup. First of all such effects cancel in the ratio Eq. 1. Furthermore, the angle Φ does not correspond to a specific azimuthal direction in the laboratory system. In the laboratory, the whole system shown in Fig.2 can be arbitrarily rotated around the beam axis, so that for each value of Φ the experiment averages automatically over all azimuthal orientations in the detector system. Any effects from the dependence of the experimental detection efficiency on the azimuthal angle in the detector frame are thus eliminated.

For the most basic version, defined as in [35,36], we choose the outgoing recoil nucleon as particle p_3 , spanning together with the photon the reaction plane, while the two pions are chosen as particles p_1 , p_2 and span the production plane. The definition of the angle Φ depends then still on the ordering of the pions, for which we can use different prescriptions. For the non-identical pions in the $N\pi^0\pi^\pm$ final state the most natural ordering is by their charge. For this we use the same convention as in [35], i.e., $p_1 = \pi^\pm$ is the charged pion and $p_2 = \pi^0$ the neutral one (this analysis is called ‘charge ordered’), the corresponding asymmetry is denoted as $I_{1c}^\odot(\Phi_{1c})$. We can also order them by the reaction kinematics, which is the only possibility for identical pions. For this we use the same condition as for the doubly neutral pairs in [15], where the pion with the larger pion-nucleon invariant mass is chosen as p_1

$$m(\pi_1, N') \geq m(\pi_2, N') \quad (2)$$

and the results, $I_{1m}^\odot(\Phi_{1m})$, are labeled ‘mass ordered’.

There are actually further asymmetries, which have not been considered in previous analyses. They arise when we choose one of the pions as p_3 . We use the following definitions. The asymmetry $I_{2c}^\circ(\Phi_{2c})$ corresponds to the choice $(p_1, p_2, p_3) = (\pi^0, N', \pi^\pm)$ and $I_{3c}^\circ(\Phi_{3c})$ to $(p_1, p_2, p_3) = (\pi^\pm, N', \pi^0)$.

Due to parity conservation all asymmetries must obey the condition:

$$I^\circ(\Phi) = -I^\circ(2\pi - \Phi).$$

For the extraction of $I^\circ(\Phi, \Theta_{\pi_1}, \Theta_{\pi_2}, \dots)$ in a limited region of kinematics, the differential cross sections $d\sigma^\pm$ can be replaced by the respective count rates N^\pm (right hand side of Eq. 1), since all normalization factors cancel in the ratio. For angle-integrated asymmetries, efficiency-weighted count rates N/ϵ should be used in the integration.

Due to their symmetry properties, the I° can be expanded in sine series

$$I^\circ(\Phi) = \sum_{n=1}^{\infty} A_n \sin(n\Phi) \quad (3)$$

which can be fitted to the data. The coefficients with even numbers must be identical (within uncertainties) for the asymmetries I_{1c}° and I_{1m}° ('charge' or 'mass' ordering of the pions in one plane), while the odd coefficients depend on the ordering (and have to vanish for 'random' ordering).

3 Experimental setup

The experiments were performed at the tagged photon facility of the Mainz Microtron accelerator MAMI [39,40]. Longitudinally polarized electron beams with energies of ≈ 1.5 GeV (see Table 1 for details) were used to produce bremsstrahlung photons in a copper radiator of 10 μm thickness, which were tagged with the upgraded Glasgow magnetic spectrometer [41,42,43]. The typical bin width for the photon beam energy (4 MeV) was defined by the geometrical size of the plastic scintillators in the focal plane detector of the tagger. The polarization degree of the electron beams was measured by Mott and Møller scattering. Their longitudinal polarization is transferred in the bremsstrahlung process to circular polarization of the photons. The polarization degree of the photon beams follows from the polarization degree of the electrons and the energy-dependent polarization transfer factors given by Olsen and Maximon [44]. The beam-helicity asymmetry can then be measured by comparing the event rates for the two helicity states of the beam. The size of the tagged photon beam spot on the targets was restricted to ≈ 1.3 cm diameter by a collimator (4 mm diameter) placed downstream from the radiator foil. The targets were Kapton cylinders of ≈ 4 cm diameter and different lengths filled with liquid hydrogen or liquid deuterium. Contributions from the target windows ($2 \times 120 \mu\text{m}$ Kapton) were determined with empty target measurements, but are negligible for the results discussed in this paper. Data were taken

during four different beam times. Their main parameters are summarized in Table 1.

Table 1. Summary of data samples. Target type (LD_2 : liquid deuterium, $\rho_d = 0.169 \text{ g/cm}^3$; LH_2 : liquid hydrogen, $\rho_H = 0.071 \text{ g/cm}^3$), target length ℓ [cm], target surface density ρ_s [nuclei/barn], electron beam energy E_{e^-} [MeV], degree of longitudinal polarization of electron beam P_{e^-} [%].

Target	ℓ [cm]	ρ_s [barn $^{-1}$]	E_{e^-} [MeV]	P_{e^-} [%]
LD_2	4.72	0.231 ± 0.005	1508	61 ± 4
LD_2	4.72	0.231 ± 0.005	1508	84.5 ± 6
LD_2	3.00	0.147 ± 0.003	1557	75.5 ± 4
LH_2	10.0	0.422 ± 0.008	1557	75.5 ± 4

Photons, charged pions, and recoil nucleons produced in the target were detected with an almost 4π electromagnetic calorimeter schematically shown in Fig. 3. It combined the Crystal Ball detector (CB) [45] with the TAPS detector [46,47]. The CB is made of 672 NaI crystals and

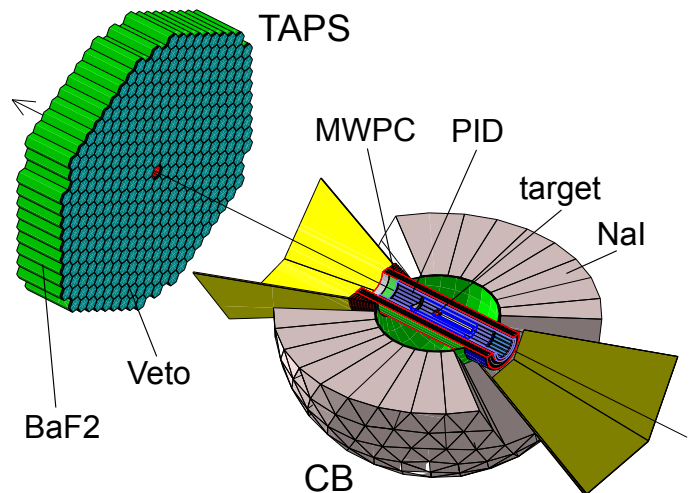


Fig. 3. Experimental setup of Crystal Ball (only bottom hemisphere shown) with PID detector and TAPS forward wall.

covers the full azimuthal range for polar angles from 20° to 160° , corresponding to 93% of the full solid angle. It is arranged in an upper and lower hemisphere (only the lower hemisphere is shown in Fig. 3). The TAPS detector, consisting of 384 BaF_2 crystals, was configured as a forward wall, placed 1.457 m downstream from the targets, and covered polar angles from $\approx 5^\circ$ to $\approx 21^\circ$. The Crystal Ball was equipped with a Particle Identification Detector (PID) [48] for the identification of charged particles and all modules of the TAPS detector had individual plastic scintillators in front for the same purpose (TAPS 'Veto-detector'). This setup is similar to the one described in more detail in [14,49] (the only difference is the size and position of the TAPS forward wall) and identical to

the setup used for the measurement of the double- π^0 final state [15].

The trigger conditions varied for the four beam times. They were optimized for different reaction types ranging from low-multiplicity final states like single π^0 production, or even Compton scattering, to high-multiplicity states like production of π^0 pairs or $\eta \rightarrow 3\pi^0 \rightarrow 6\gamma$ decays. They were always based on the multiplicity of hits in the combined calorimeter and the analog sum of the energy signals from detector modules of the Crystal Ball. For the multiplicity information, both calorimeters were subdivided into logical sectors. The TAPS detector was divided into 6×64 modules in a pizza-like geometry (i.e. into 6 triangularly shaped sectors pointing to the beam pipe) and the CB into 45 rectangular sectors (each composed of 16 detector modules of triangular cross section). The different triggers required hits in 1 - 3 logical sectors of the combined calorimeter with analog energy sums in the CB of ≈ 300 MeV. Triggers with hit multiplicity of one or two are activated by the decay photons from the $\pi^0\pi^\pm$ final state. For multiplicity-three triggers the charged pion must also contribute, which resulted in larger systematic uncertainties for absolute cross sections. One should, however, keep in mind that such uncertainties (also from the exact definition of the analog sum threshold of the CB) cancel in the asymmetries discussed in this paper.

4 Data analysis

The reactions analyzed were $\gamma p \rightarrow n\pi^0\pi^+$ (photoproduction off free protons), $\gamma d \rightarrow (n)n\pi^0\pi^+$ (photoproduction off quasi-free protons bound in the deuteron), and $\gamma d \rightarrow (p)p\pi^0\pi^-$ (photoproduction off quasi-free neutrons bound in the deuteron). The nucleon in brackets is the spectator, the other nucleon the participant in the final state (the initial-state participant has of course the other charge). Detection of the participant recoil nucleon is mandatory for reactions measured with the deuteron target. Therefore, detection of the recoil neutron was also required for the measurement with the hydrogen target so that the analysis for both targets was identical. This means that for all reactions, the accepted events were those with candidates for two photons from the π^0 decay, a candidate for a charged pion, and a candidate for either a recoil proton (only for the deuteron target) or a recoil neutron.

The analysis combined the particle identification possibilities of the detector (charged particle identification, pulse-shape analysis (PSA) in TAPS, time-of-flight (ToF) versus energy in TAPS, and $\Delta E - E$ analysis of CB and PID; see [14,49] for details) with the reaction identification via invariant-mass analyses, meson-pair nucleon coplanarity, and missing-mass analyses. The separation of photons and recoil nucleons in TAPS via PSA and the separation of recoil protons and charged pions in the CB-PID system by the $\Delta E - E$ analysis is shown in Fig. 4. For both reactions, the first step of the analysis used the charged-particle identification sub-detectors (TAPS-‘Veto’ and PID) to assign hits in the calorimeter parts

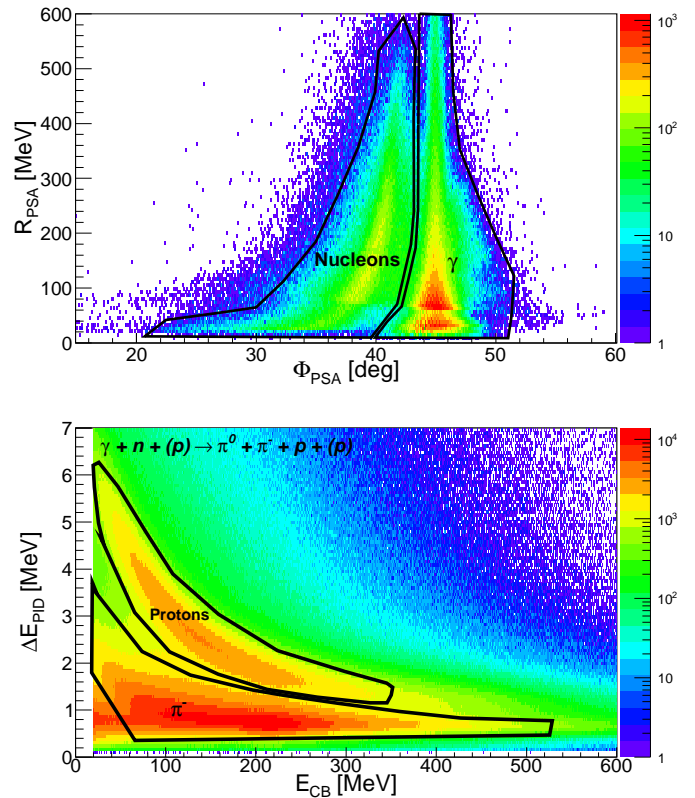


Fig. 4. Upper panel: pulse-shape analysis in TAPS for one individual detector module. Plotted is the radius R_{PSA} versus the angle Φ_{PSA} of the polar-coordinate parameterization of the pulse-shape like in Ref. [14]. Lower panel: $\Delta E - E$ analysis with PID and CB. Energy deposited in the PID scintillators as function of the energy deposited in the CB. Separation of protons and charged pions for candidates of the $\pi^0\pi^-p$ final state (two charged, two neutral hits in the calorimeter).

of the detector to ‘charged’ or ‘neutral’. Events with exactly one ‘charged’ and three ‘neutral’ hits were analyzed as candidates for the $n\pi^+\pi^0$ final state and events with exactly two ‘charged’ and exactly two ‘neutral’ hits were accepted as candidates for the $p\pi^-\pi^0$ final state.

In the next step, the neutral hits were inspected more closely. For assumed $p\pi^-\pi^0$ events it was required that the candidates for the π^0 -decay photons, when detected in TAPS, passed the PSA filter as photons. For candidates of $n\pi^+\pi^0$ with three neutral hits, a χ^2 test was first used to identify the most probable combination of the three neutral hits to decay photons of a π^0 meson and a neutron. This was done by minimizing

$$\chi^2 = \frac{(m_{\gamma\gamma}(k) - m_{\pi^0})^2}{\Delta m_{\gamma\gamma}(k)} \quad k = 1, 2, 3$$

where $m_{\gamma\gamma}(k)$ are the invariant masses of the three possible combinations of neutral hits to pion-decay photons, $\Delta m_{\gamma\gamma}(k)$ are their uncertainties, and m_{π^0} is the nominal pion mass. The two neutral hits of the ‘best’ combination were taken as photon candidates, leaving the third hit as a neutron candidate. Subsequently, for neutral hits in TAPS

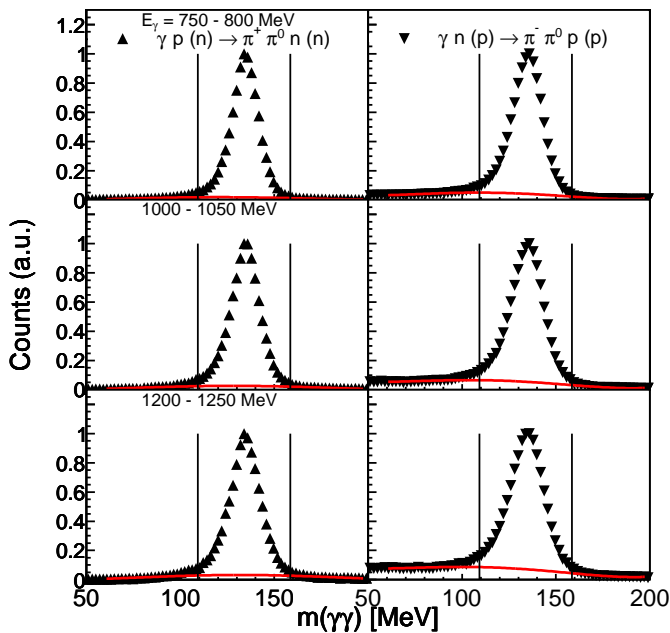


Fig. 5. Invariant-mass distribution of the candidates for two-photon decays of the π^0 . Left hand side: $\pi^+\pi^0n$, right hand side: $p\pi^-\pi^0$. For the $\pi^+\pi^0n$ final state the ‘best’ $\gamma\gamma$ -pair is selected by the χ^2 test. The two vertical lines indicate the accepted range. The red line is a polynomial fit to the background.

it was checked whether hits assigned as photons passed the PSA analysis cuts for photons and hits assigned to neutrons passed the neutron PSA cut. For neutral hits in the CB no additional conditions could be applied. The resulting invariant-mass spectra for both reaction channels are summarized in Fig. 5. The background level is very low. For both reactions entries with invariant masses between 110 MeV and 160 MeV were accepted.

The nominal invariant mass m_{π^0} of the π^0 meson was then used to improve the experimental resolution further. Since for both sub-calorimeters the angular resolution is better than the energy resolution, this was simply done by replacing the measured energies E_i of the photon hits by

$$E'_i = E_i \frac{m_{\pi^0}}{m_{\gamma\gamma}} \quad i = 1, 2$$

where $m_{\gamma\gamma}$ are the measured invariant masses.

Subsequently, the candidates for protons and charged pions were analyzed. The separation of protons and charged pions in CB with help of the CB-PID $\Delta E - E$ analysis was very efficient, but the separation in TAPS via ToF versus energy was not as good. Due to the high intensity in the proton band (partly from background reactions) the pion band in ToF versus energy was contaminated with protons. Therefore, events with the charged pion candidate in TAPS were not included in the analysis. The result is that a small part of the reaction phase-space (polar laboratory angles of charged pion $< 20^\circ$) was excluded. This is only a small effect, but must be taken into account when the results are compared to model predictions. Events accepted

for $n\pi^+\pi^0$ were those with the charged pion identified in the CB via $\Delta E - E$. For $p\pi^-\pi^0$ events, it was required that the charged pion satisfied the $\Delta E - E$ condition and that the other charged hit (proton candidate) when detected in the CB passed the $\Delta E - E$ analysis as proton, or, when in TAPS, passed the PSA filter as nucleon.

For events detected in TAPS, the ToF-versus-energy spectra served as a final test for the particle identification. Such spectra are summarized in Fig. 6 and show the expected behavior: photon candidates form a band at constant ToF corresponding to the (normalized) target - detector distance. Protons are lying in a band matching the relativistic ToF-energy relation for kinetic energies below ≈ 400 MeV. For higher kinetic energies, the band bends back because the protons are no longer stopped in the BaF₂ crystals but punch through the backside of the detector. Neutrons deposit a random fraction of their kinetic energy and thus appear in the region below the proton band. Since no significant background structures were observed in these spectra, no cuts were applied in order to avoid unnecessary systematic uncertainties related to the cuts. Cutting roughly on the signal regions in the spectra has no effect on the results.

Altogether, at this stage of analysis, the identification of the different particle types with partly redundant filters is excellent. However, there is still background from competing reactions where some final-state particles escaped detection. These are, for example, events from triple-pion production (a significant fraction stems from the $\eta \rightarrow \pi^0\pi^+\pi^-$ decay), where one charged pion was too low in energy for detection or went along the beam-pipe.

Such background must be eliminated using the overdetermined reaction kinematics. As a first step, the coplanarity of the meson pairs with the recoil nucleon was analyzed. The sum of the three-momentum components of the $N\pi\pi$ final-state particles perpendicular to the beam axis must vanish (apart from effects from Fermi motion, which broaden the distributions). Figure 7 shows the azimuthal angular difference $\Delta\Phi$ of the three-momenta of the two-pion system and the recoil nucleon in the cm system together with Monte Carlo (MC) simulations of the expected signal shape and background contributions. Only events with $\Delta\Phi$ in the range $(180 \pm 20)^\circ$ were accepted. This cut removes mainly background for the reaction with coincident recoil neutrons, but cannot completely suppress it since some background contributions such as events from $\eta \rightarrow 3\pi$ also peak at 180° . For the $\pi^-\pi^0p$ final state this is the dominant background contribution (mainly arising from the final state $n\pi^0\pi^+\pi^-$ when the recoil neutron escapes detection and one of the charged pions is misidentified as a proton). However, this background is subsequently removed by the more efficient missing-mass analysis (see below).

In the final analysis step the recoil nucleons, although detected, were treated as missing particles and their mass m_N was compared to the mass reconstructed from the incident photon energy and the four-vectors of the two pions via

$$\Delta M = |P_\gamma + P_N - P_{\pi^0} - P_{\pi^\pm}| - m_N \quad (4)$$

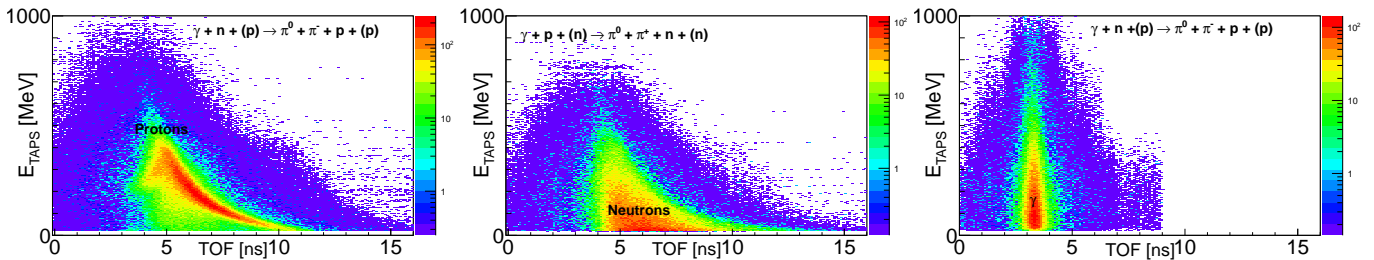


Fig. 6. ToF-versus-energy spectra for hits in TAPS assigned to (from left to right) proton, neutron and photon candidates.

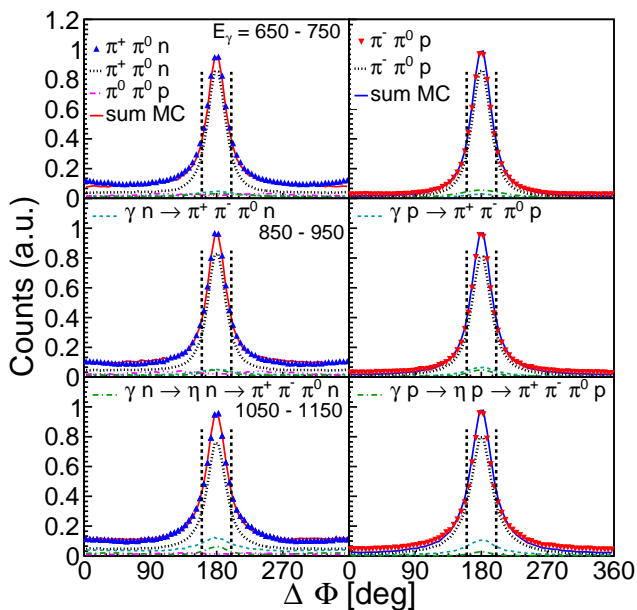


Fig. 7. Spectra of the azimuthal difference between the cm three-momenta of the two-pion system and the recoil nucleon. Left panel: recoil neutrons, right panel: recoil protons. Triangles: measured data, curves: MC simulations of signal and background components.

where P_γ , P_N are the four-vectors of incident photon and incident nucleon (assumed to be at rest, with the distribution again broadened by Fermi motion), and P_{π^0} , P_{π^\pm} are the four-momenta of the pions. The result of this analysis is summarized in Fig. 8 and compared to simulations of the signal shape and background from triple-pion production either from the η -decay or from phase-space contributions which are the main background sources. In case of the $\pi^0\pi^+n$ final state there is also a small background component from the $\gamma p \rightarrow \pi^0\pi^0p$ reaction with one undetected photon, the proton misidentified as charged pion, and one photon misidentified as a neutron. The sum of the MC simulations for signal and background does a good job of reproducing the measured data. For the construction of the asymmetries events were only accepted in the ΔM range (-80 MeV to $+80$ MeV) for which the simulations indicated very small background. The cut at -80 MeV does not improve the peak-to-background ratio but avoids systematic effects from Fermi motion. With an asymmetric cut, one would select a biased momentum distribution of

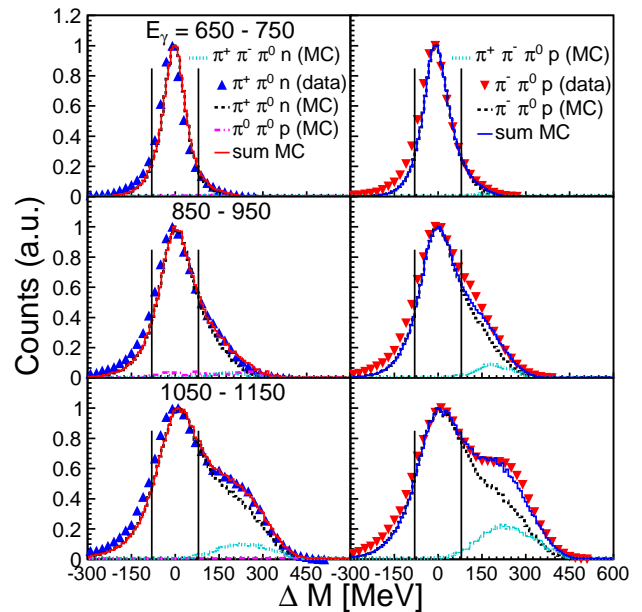


Fig. 8. Missing-mass distribution for three typical ranges of E_γ . Left column: (blue) triangles experimental results for $\pi^0\pi^+n$ final state. Dotted (black) lines: MC signal, (light blue) lines: MC background from triple pion production, (magenta) lines: MC background from $\pi^0\pi^0p$, solid (red) lines: sum of MC signal and MC backgrounds, vertical (black) lines: applied cut. Right column: (red) triangles: experimental results for $\pi^0\pi^-p$ final state. Solid (blue) lines: sum of MC signal and backgrounds.

the nucleons (preferring nucleon momenta antiparallel to the photon momentum). Since the statistical quality of the data is excellent, the small loss in counting statistics did not matter.

In order to remove completely the influence of nuclear Fermi motion, the invariant mass W of the $N_p\pi\pi$ final state (N_p : participant nucleon) for quasi-free production off the deuteron was derived event-by-event from the four-momenta of the three particles. The three momenta of the pions were directly measured with the calorimeter. Azimuthal and polar angles for all recoil nucleons were measured with good resolution. In principle, kinetic energies of recoil nucleons detected in TAPS can be reconstructed from ToF. Kinetic energies of protons up to ≈ 400 MeV (at higher energies they are not stopped) can be extracted from their deposited energies. However, for the recoil neu-

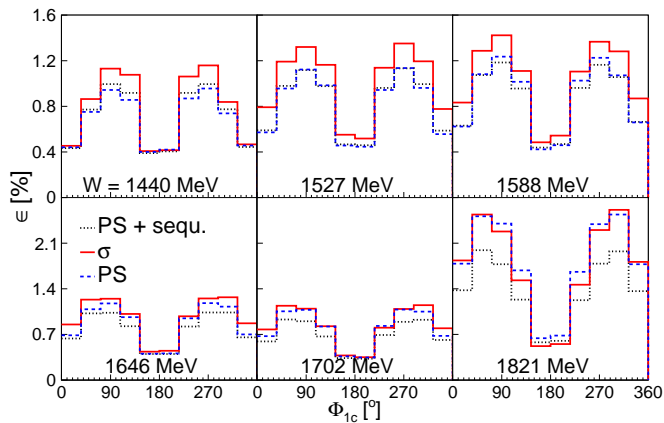


Fig. 9. Simulated detection efficiency as function of the angle Φ_{1c} for different bins of final state invariant mass for the reaction $\gamma p \rightarrow n\pi^0\pi^+$ for the free proton target. Solid (red) histograms: event generator from model [22], dashed (blue): phase-space, dotted (black): phase space and sequential decays via $\Delta(1232)$ intermediate state.

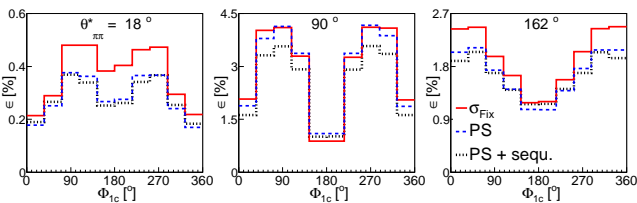


Fig. 10. Same as Fig. 9 but for different bins of the polar angle of the parent particle of the two pions (i.e. $180^\circ - \Theta_N^*$).

trons registered in the CB only the angles were available. Therefore, in order to minimize systematic effects, all quasi-free recoil nucleons were treated in the same way and only the measured polar and azimuthal angles were used in the analysis. The kinetic energies were then reconstructed from energy and momentum conservation as discussed in [37,38]. For the measurement with free protons, W was calculated from the incident photon energy.

Asymmetries for a narrowly restricted range of kinematic variables can be constructed from the measured count rates according to Eq. 1 because all normalization factors such as photon flux, target density, and detection efficiency cancel in the ratio. However, variations of the detection efficiency can matter for asymmetries integrated over angles and/or incident photon energies. Particularly, the detection efficiency of recoil nucleons varies systematically with their kinetic energies and thus also with their polar angles. Therefore, the detection efficiency was simulated with the Geant4 code [50], taking into account all details of the setup. The measured data and also the simulated events were analyzed in bins of the final state invariant mass W , the angle Φ between the two planes (see Fig. 2), and the cm polar angle of the two-pion system $\Theta_{\pi\pi}^* = 180^\circ - \Theta_N^*$, where Θ_N^* is the cm polar angle of the recoil nucleon. The measured count rates for the three-dimensional cells were then corrected by the simulated detection efficiencies for the same cells, projected onto the

Θ^* axis, and into the bins of W specified in the figures. Subsequently, the integrated asymmetries were calculated with Eq. 1. Since photoproduction of pion pairs involves five independent kinematic variables [31], and the detection efficiency was corrected only in a three-dimensional space (spanned by the three most important variables), the result depends in principle on the event generator used for the MC simulations. Three different event generators were tested. The most simple one used a phase-space distribution of events. The second one used a mixture of phase space and the reaction chains $\gamma N \rightarrow \pi^0\Delta(1232) \rightarrow \pi^0\pi^\pm N$ and $\gamma N \rightarrow \pi^\pm\Delta(1232) \rightarrow \pi^\pm\pi^0 N$, where the relative size of the contributions from the three processes were fixed by fits of the pion-pion and pion-nucleon invariant mass distributions. The third one used the distributions from the Two-Pion-MAID model [22].

Typical examples of the simulated efficiencies for the reaction $\gamma p \rightarrow n\pi^0\pi^+$ are shown in Fig. 9 for bins of the final state invariant mass W , and in Fig. 10 for bins of the cm polar angle $\Theta_{\pi\pi}^*$ of the two-pion system, both as function of the angle Φ_{1c} (all other kinematic parameters integrated out). The efficiencies generated with the different inputs differ in absolute magnitude. However, the magnitude of the detection efficiencies and their variation with Φ does not matter here because they cancel in the ratio (see Eq. 1). Only their variation with other kinematic parameters, which have been integrated out, could matter when the asymmetry changes significantly with them. But these effects turn out to be small. As an example, the results for $I_{1c}^\circ(\Phi_{1c})$ for $\gamma p \rightarrow n\pi^0\pi^+$ for the free proton target extracted with the different detection efficiencies are compared in Fig. 11. Also shown in the figure are asymmetries extracted without *any* correction for detection efficiency. The results are very similar, demonstrating that the efficiency corrections are not critical. The main effects from the detection efficiency cancel in the ratio; even for the angle integrated count rates. Effects from detection efficiency are also small for the other reactions and asymmetries. All results discussed below have been obtained with an efficiency correction using the phase-space event generator.

In the following section, only statistical uncertainties are plotted for all results. The use of Eq. 1 assumes of course that the incident photon flux is equal for both polarization states of the beam. The polarization state was switched in a randomized way with a frequency of 1 Hz. Possible differences in the numbers of incident photons for the two helicity states have been determined to be at the 5×10^{-4} level, i.e. they are negligible here. The polarization degree of the electron beam was measured with uncertainties between 5% and 7%, uncertainties arising from the above efficiency correction are estimated below the 5% level, and possible residual background contributions at maximum W are estimated at the 5% level (they are negligible for the lowest W values).

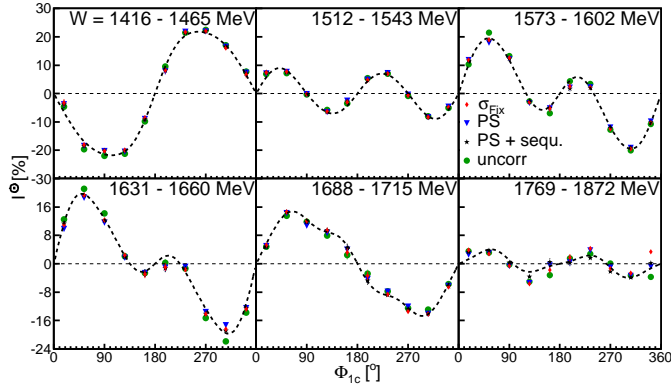


Fig. 11. Asymmetry $I_{1c}^\ominus(\Phi_{1c})$ for $\gamma p \rightarrow n\pi^0\pi^+$ for the free proton target and with different detection efficiency corrections. Color code like in Figs. 9,10 and additionally (filled, green circles) without any efficiency correction. Dotted lines: fits to data (black stars). All uncertainties only statistical.

5 Results

Before we summarize and discuss the extracted asymmetries some remarks to their internal consistency and a comparison to the existing data base are appropriate.

As mentioned in Section 2 parity conservation requires that all asymmetries respect Eq. 3. This condition can be used as an independent test of systematic uncertainties. All data sets respect this relation within experimental uncertainties, most already within statistical uncertainties. As an example we show in Fig. 12 for a few energy bins the asymmetry $I_{1c}^\ominus(\Phi_{1c})$ for quasi-free protons and quasi-free neutrons. At the left hand side of the figure $I_{1c}^\ominus(\Phi_{1c})$ is compared to the mirrored values $-I_{1c}^\ominus(360^\circ - \Phi_{1c})$ and at the right hand side the sum $I_{1c}^\ominus(\Phi_{1c}) + I_{1c}^\ominus(360^\circ - \Phi_{1c})$ is shown. The magnitude of the asymmetry is substantial and the sum of original and mirrored values is consistent with zero. No systematic discrepancies between the $\Phi = 0^\circ - 180^\circ$ and the $\Phi = 180^\circ - 360^\circ$ data were observed and thus no indication for false, detector related asymmetries was found.

Previous results are only available for the asymmetry $I_{1c}^\ominus(\Phi_{1c})$ for the free proton target and incident photon energies below 820 MeV [35]. They are compared in Fig. 13 to the present data. The two data sets are in reasonable agreement, but the previous data have much better statistical quality. Small systematic discrepancies might arise from the different analysis strategies: unlike in the present analysis, in Ref. [35] detection of the recoil proton was not required, which removes one source of possible systematic effects. Detection efficiency effects were not considered in [35], but as discussed above they seem to be negligible. One should also note that the lowest energy bins shown in this figure are at the very limit accessible by the present experiment (mainly due to the trigger conditions which required an energy deposition of 300 MeV in the Crystal Ball), while the previous experiment was optimized for the low energy range.

In the following we summarize the most relevant results from the large body of data obtained by the present

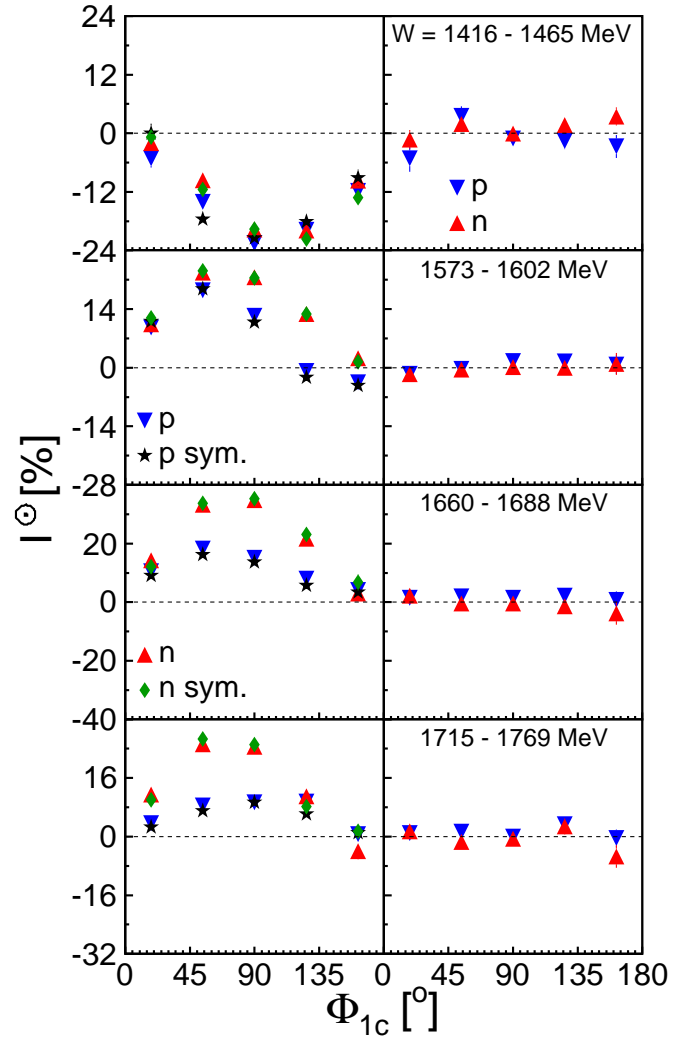


Fig. 12. Parity conservation for the asymmetries $I_{1c}^\ominus(\Phi_{1c})$. Left hand side: $I_{1c}^\ominus(\Phi_{1c})$, $0^\circ \leq \Phi_{1c} \leq 180^\circ$ for $\gamma p \rightarrow n\pi^0\pi^+$ (blue, down pointing triangles) and for $\gamma n \rightarrow p\pi^0\pi^+$ (red, up pointing triangles) compared to $-I_{1c}^\ominus(360^\circ - \Phi_{1c})$ (black stars for $\gamma p \rightarrow n\pi^0\pi^+$, green diamonds for $\gamma n \rightarrow p\pi^0\pi^+$). Right hand side: $I_{1c}^\ominus(\Phi_{1c}) + I_{1c}^\ominus(360^\circ - \Phi_{1c})$, $0^\circ \leq \Phi_{1c} \leq 180^\circ$ for $\gamma p \rightarrow n\pi^0\pi^+$ (blue, down pointing triangles) and $\gamma n \rightarrow p\pi^0\pi^+$ (red, up pointing triangles).

experiment. The asymmetries $I_{1c}^\ominus(\Phi_{1c})$ and $I_{1m}^\ominus(\Phi_{1m})$ for the ‘charge’ and ‘invariant-mass’ ordering of the pions for the free proton measured with the hydrogen target and the quasi-free protons and neutrons from the deuterium target are shown for the full range of measured photon energies in Figs. 14 and 15. The three different ‘charge ordered’ asymmetries $I_{1c}^\ominus(\Phi_{1c})$, $I_{2c}^\ominus(\Phi_{2c})$, and $I_{3c}^\ominus(\Phi_{3c})$ corresponding to $(p_1, p_2, p_3) = (\pi^\pm, \pi^0, N')$, (π^0, N', π^\pm) , and (π^\pm, N', π^0) are compared in Fig. 16 (for $\gamma p \rightarrow n\pi^0\pi^+$) and Fig. 17 (for $\gamma n \rightarrow p\pi^0\pi^+$). These data are for quasi-free production from nucleons bound in the deuteron.

All discussed asymmetries have been integrated over the the full reaction phase-space with the exception of events where the charged pion was emitted to laboratory polar angles smaller than 20° (i.e. into the angular range

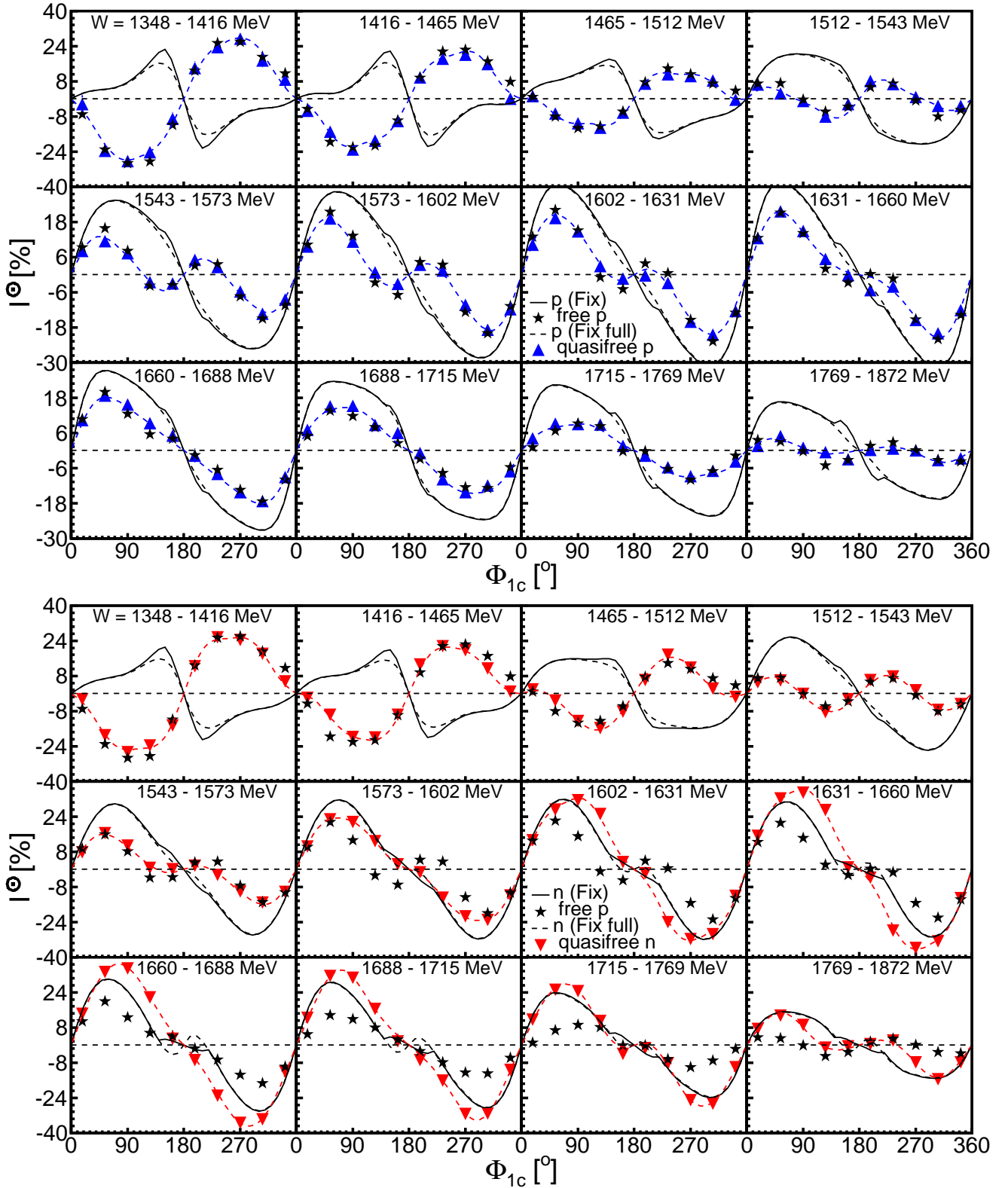


Fig. 14. Results for ‘charge-ordered’ $I_{1c}^\ominus(\Phi_{1c})$ for different ranges of $W = \sqrt{s}$. Upper block: (black) stars: free proton, (blue) triangles: quasi-free proton. Dashed (blue) curves: fits to quasi-free proton data with Eq. 3. (Black) solid curves: model results from [22] taking into account experimental acceptance. (Black) dashed: model results without acceptance restriction. Lower Block: data for quasi-free neutrons (red) triangles compared to free proton. Dashed (red) curves: fits to neutron data. Solid, dashed (black) curves: model results from [22].

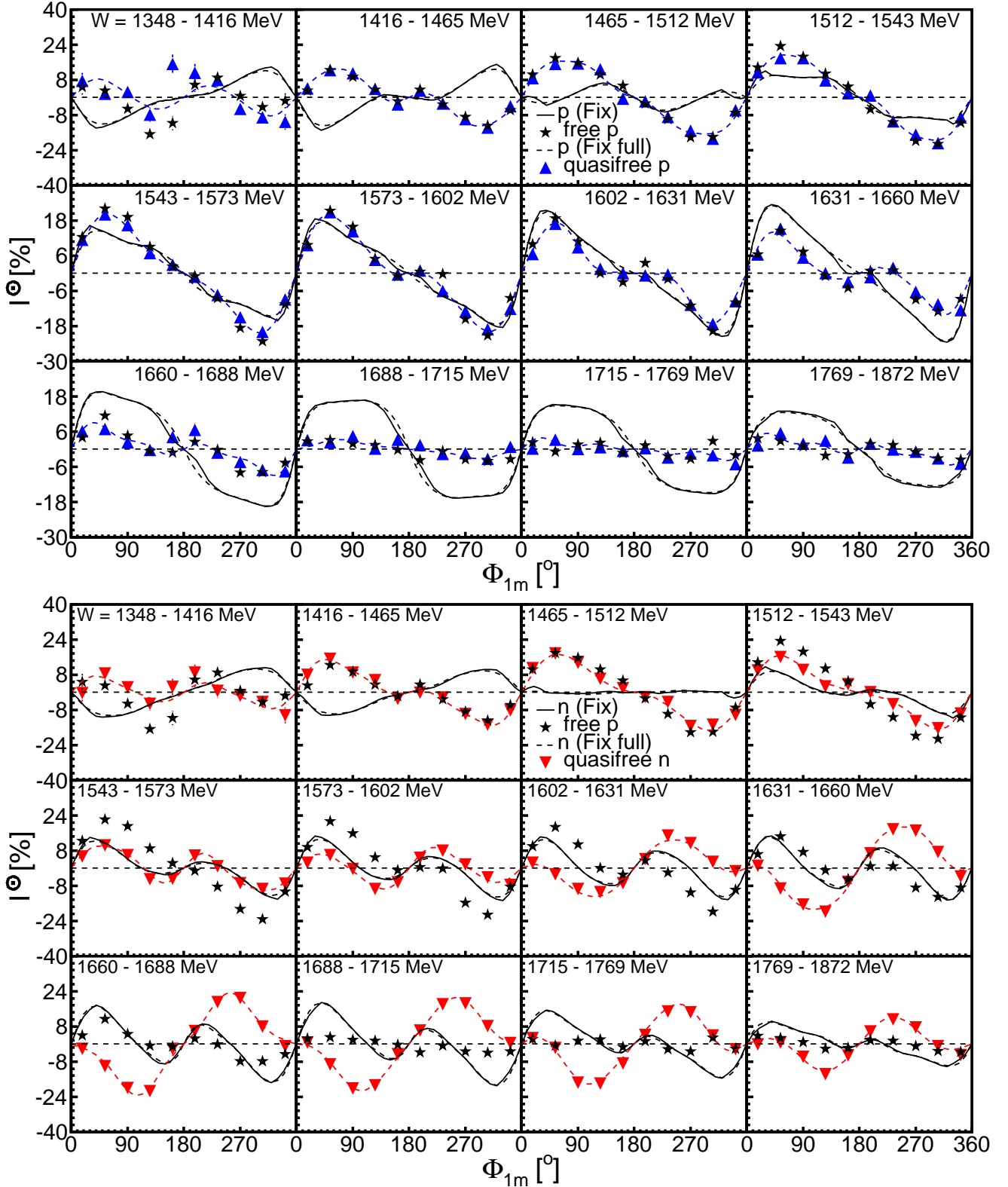


Fig. 15. Results for ‘mass-ordered’ $I_{1m}^{\odot}(\Phi_{1m})$ for different ranges of $W = \sqrt{s}$. For labeling see Fig. 14.

covered by TAPS). The predictions from the Two-Pion-MAID model [22] are compared in all figures to the data.

The distributions have been fitted with the sine-series from Eq. 3. The results of the fits for the coefficients are

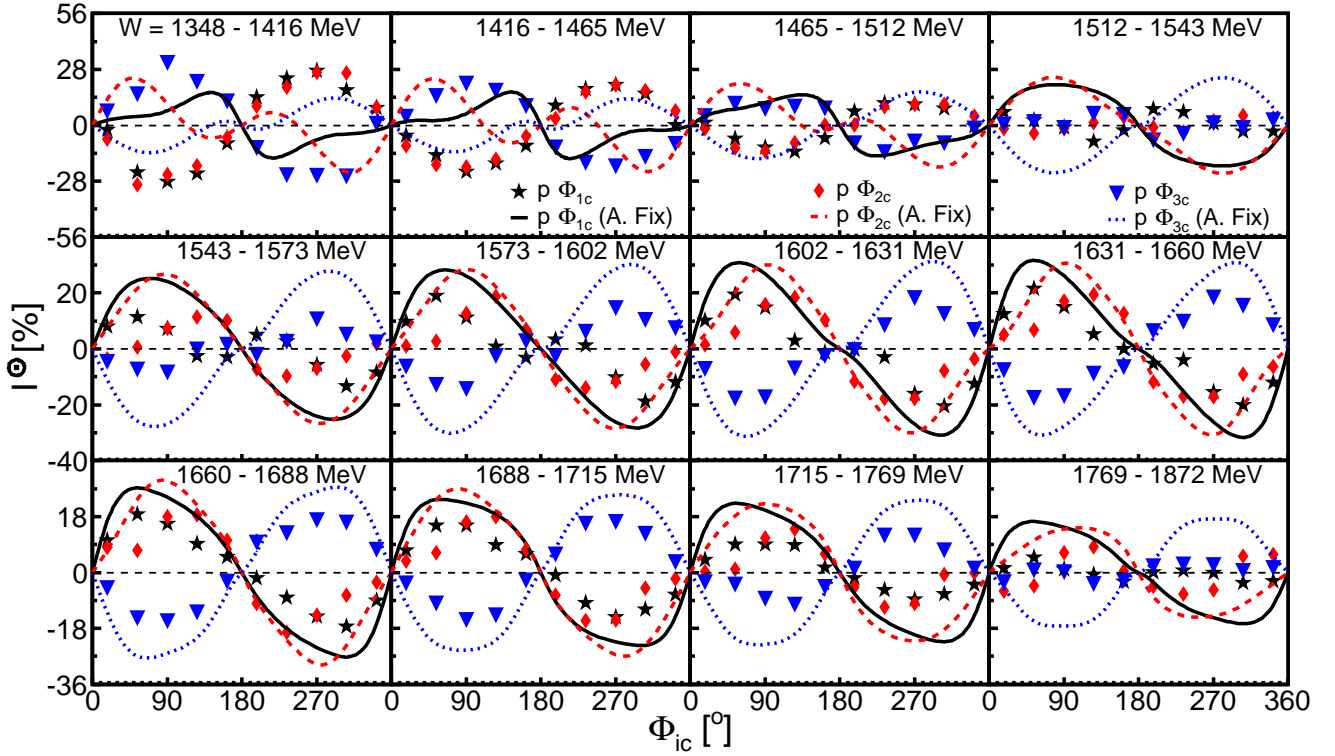


Fig. 16. Results for $I_{1c}^{\odot}(\Phi_{1c})$ (black stars, black solid lines), $I_{2}^{\odot}(\Phi_{2})$ (red diamonds, dashed red lines), and $I_{3}^{\odot}(\Phi_{3})$ (blue triangles, blue dotted lines) for the $\gamma p \rightarrow n\pi^0\pi^+$ reaction. The symbols represent the data, the lines are the predictions from the Two-Pion-MAID model [22].

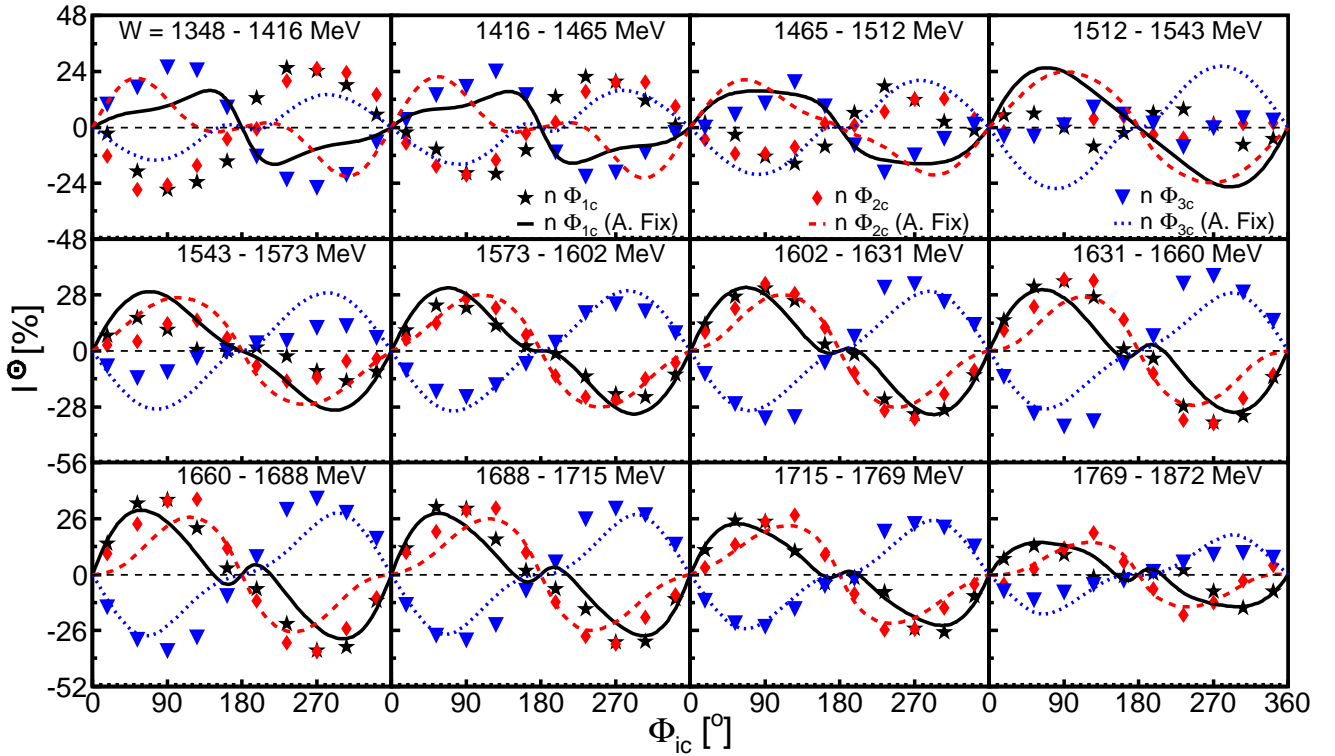


Fig. 17. Same as Fig. 16 for the $\gamma n \rightarrow p\pi^0\pi^-$ reaction.

summarized and compared to the model predictions from [22] in Figs. 18-21.

The free-proton data as well as the quasi-free proton and quasi-free neutron data were analyzed as a func-

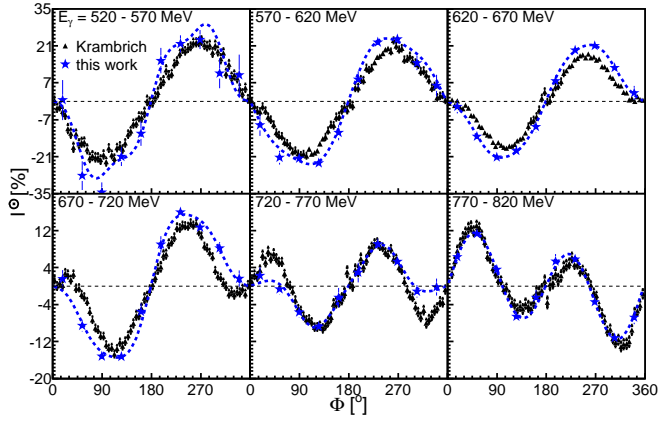


Fig. 13. Asymmetries (‘charge-ordered’) for the free proton (blue stars, present experiment) compared to previous results (black triangles) [35]. Dashed curve: fits to the data with Eq. 3.

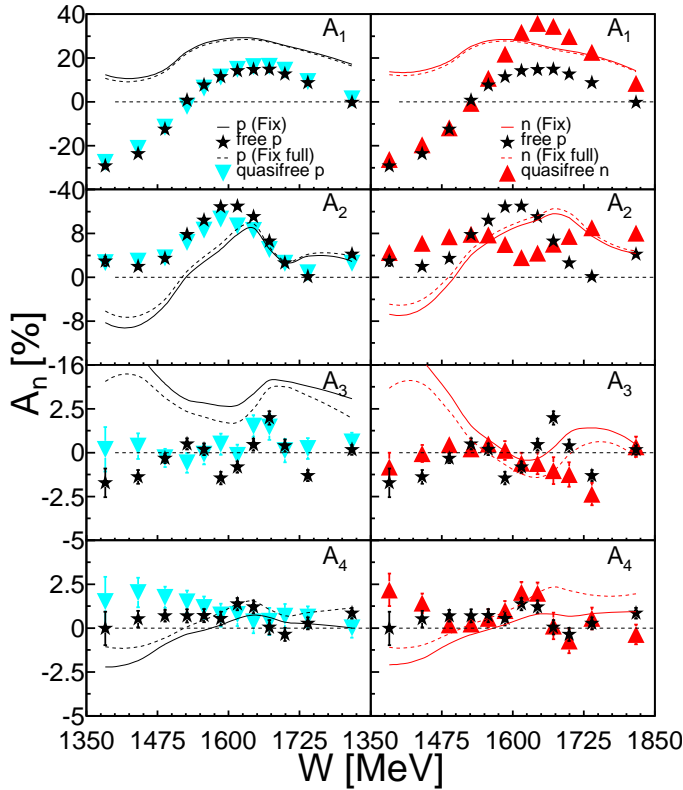


Fig. 18. Coefficients of the fits of the ‘charge-ordered’ asymmetries $I_{1c}^O(\Phi_{1c})$ from Fig. 14 with Eq. 3 as function of cm-energy W . Left hand side: free and quasi-free proton data, right hand side: comparison of proton and neutron asymmetries. Solid curves: model results from [22] restricted to experimental acceptance. Dashed curves: same model without acceptance restriction.

tion of the final-state invariant mass W (of the two-pion-participant-nucleon system), which was reconstructed as discussed in Sec. 4. All asymmetries for the free and quasi-free proton targets agree quite well, demonstrating that the kinematic reconstruction of the final state reliably eliminates the effects of nuclear Fermi motion (within ex-

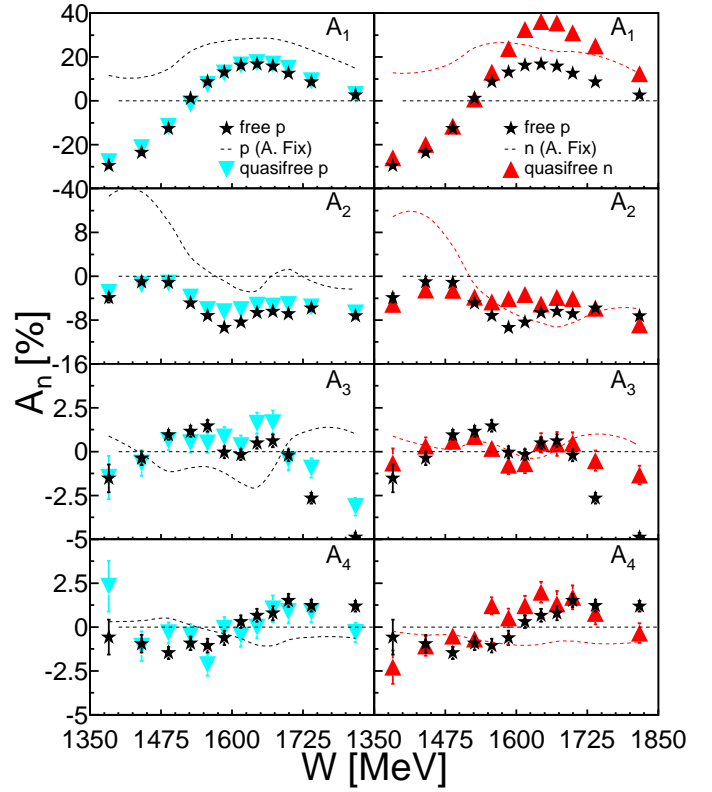


Fig. 19. Coefficients of the asymmetries $I_{2c}^O(\Phi_{2c})$. Notation as in Fig. 18.

perimental resolution). This is not trivial, Fermi motion modifies not only the effective W but influences also the orientation of the two planes and thus the angle Φ .

Also this angle must be reconstructed for the ‘true’ cm system. Analyses of the quasi-free data without careful reconstruction of the Fermi-motion related effects result in asymmetries with significantly reduced magnitudes. Further nuclear effects from final-state interactions (FSI), were not observed in the comparison of free and quasi-free proton data. This is the justification for the assumption that the quasi-free neutron data can be regarded as a close approximation of free-neutron data. The same observation has been previously made for the $\pi^0\pi^0$ final state [15]. FSI effects seem to be more important for absolute cross section data, however, even for such data they depend strongly on the reaction under study. Detailed model predictions for FSI are up to now only available for a few reaction channels. Substantial effects have been found for the $\gamma n \rightarrow p\pi^-$ reaction measured with neutrons bound in the deuteron. Their energy and angular dependence has been studied with models beyond the impulse approximation in references [53,54]. Large effects have also been found for the $\gamma N \rightarrow N\pi^0$ reactions off nucleons bound in the deuteron [55]. On the other hand, FSI effects for quasi-free photoproduction of η [56,38,58] and η' -mesons [57] off nucleons from the deuteron are negligible, while for ^3He nuclei also η -photoproduction shows large FSI [59].

The influence of the small acceptance restriction, which excluded charged pions in TAPS (i.e. at laboratory po-

lar angles below 20°) from the analysis was investigated by imposing the same restriction to the model results. Model results for 4π acceptance and for the restricted acceptance are shown in Figs. 14,15,18,21. The results are so similar that this limitation is ignored in the further discussion. One should, however, take it into account when other model results are compared to the data.

In the following we summarize the most prominent features of the data. All asymmetries are dominated by the low-order terms A_1, A_2 of the sine-expansion from Eq. 3. Magnitudes up to 40% are reached for A_1 (up to 10% for A_2), while the higher orders are in the range of a few per cent and partly at the limit of statistical significance.

Although there is no generally valid relation between the three charge ordered asymmetries $I_{1c}^\circ(\Phi_{1c})$, $I_{2c}^\circ(\Phi_{2c})$, and $I_{3c}^\circ(\Phi_{3c})$ the present results seem to obey the relation

$$A_1(I_{1c}^\circ) \approx A_1(I_{2c}^\circ) \approx -A_1(I_{3c}^\circ) \quad (5)$$

for the leading A_1 coefficient. This is true for the experimental results and also for the model predictions (although they are not in agreement with each other for the actual values of the coefficients).

Due to its symmetry, the even coefficients of the sine-series should not depend on the ordering of p_1 and p_2 i.e. they should be identical for $I_{1c}^\circ(\Phi_{1c})$ (Fig. 18) and $I_{1m}^\circ(\Phi_{1m})$ (Fig. 21) and also for a random ordering of p_1, p_2 . The odd coefficients depend on the ordering and have to vanish for random ordering. The latter condition was

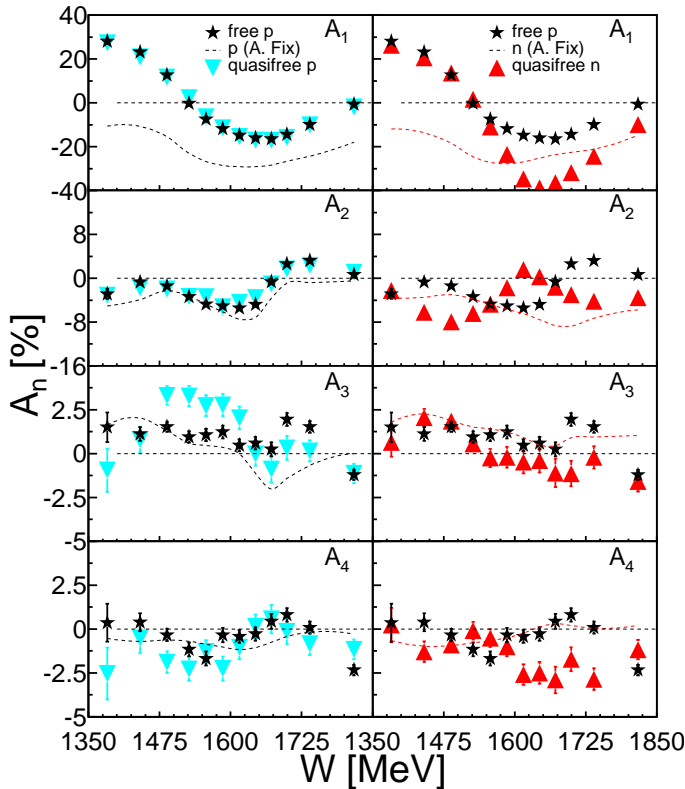


Fig. 20. Coefficients of the asymmetries $I_{3c}^\circ(\Phi_{3c})$. Notation as in Fig. 18.

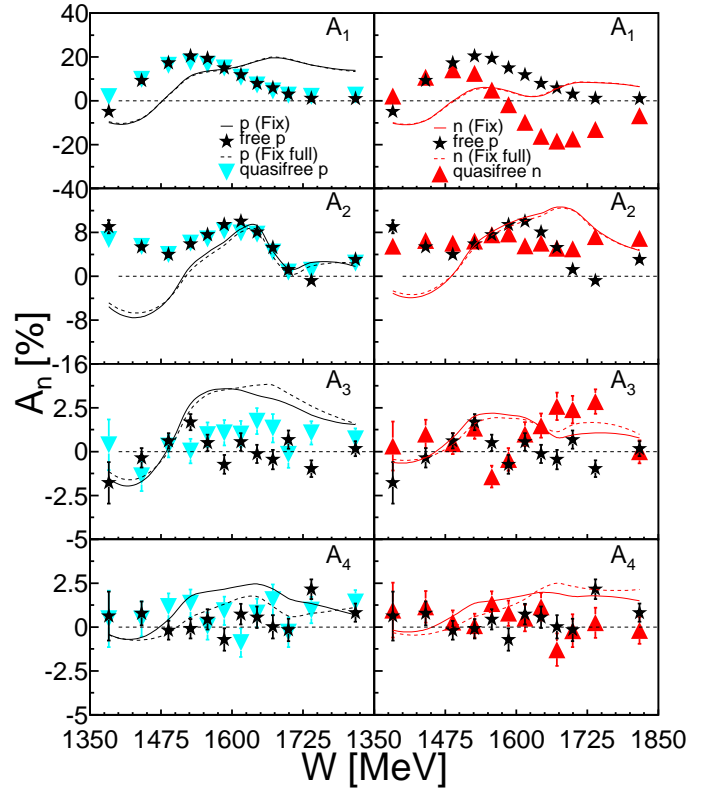


Fig. 21. Coefficients of the fits of the ‘mass-ordered’ asymmetries $I_{1m}^\circ(\Phi_{1m})$ from Fig. 15. Notation as in Fig. 18.

fulfilled within statistical uncertainties. The small A_4 coefficient agrees for $I_{1c}^\circ(\Phi_{1c})$ and $I_{1m}^\circ(\Phi_{1m})$ basically within statistical uncertainties. For the A_2 coefficient there are deviations between the two ordering schemes in particular for protons at the lowest W values. Comparison of the two data sets gives an indication for systematic uncertainties. Here one should note, that at these W values $I_{1c}^\circ(\Phi_{1c})$ is strongly dominated by the A_1 term, which almost vanishes for $I_{1m}^\circ(\Phi_{1m})$ so that probably the fit results for the smaller coefficients at low W are more reliable for $I_{1m}^\circ(\Phi_{1m})$.

The results for the proton and neutron asymmetries are similar for W below ≈ 1540 MeV, i.e. in the second resonance region, but differ significantly for larger W , in particular for the invariant mass ordering of the asymmetries. In this respect they behave differently from the previously studied $\gamma N \rightarrow n\pi^0\pi^0$ reaction [15] for which the proton and neutron asymmetries agreed over the full energy range. The behavior observed here is more in line with expectations than the $N\pi^0\pi^0$ results. In the second resonance region states like the $D_{13}(1520)$ are excited with comparable strength on protons and neutrons, which may explain the similarities. However, at larger W , in the third resonance region, the dominant resonance contributions for protons and neutrons come from different states, so that different asymmetries are to be expected.

All results discussed so far were integrated over all kinematic variables apart from the final state invariant

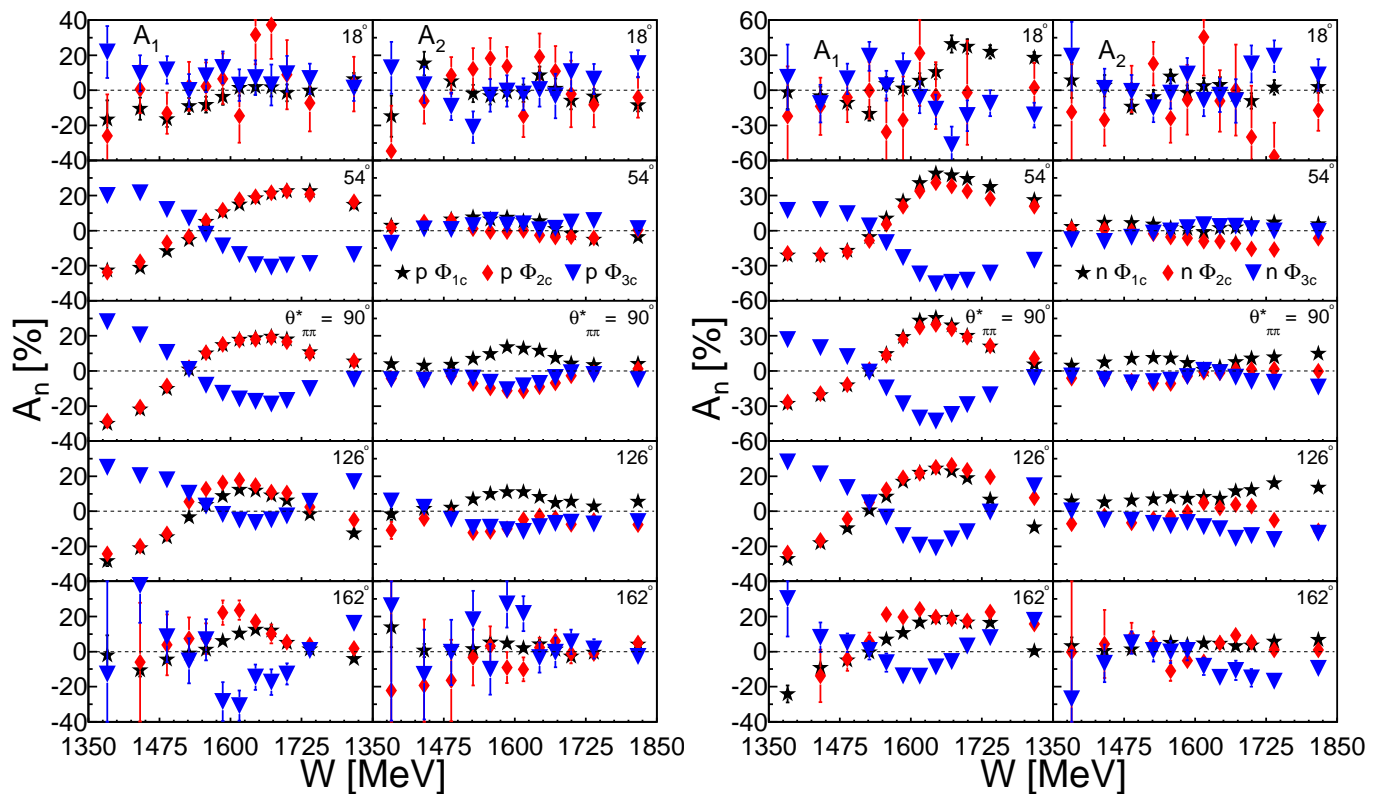


Fig. 22. Coefficients A_1 , A_2 for the asymmetries $I_{1c}^{\circ}(\Phi_{1c})$, $I_{2c}^{\circ}(\Phi_{2c})$, and $I_{3c}^{\circ}(\Phi_{3c})$ for different cm polar angles of the $\pi\pi$ system as function of W for the reactions $\gamma p \rightarrow n\pi^0\pi^+$ (left hand side) and $\gamma n \rightarrow p\pi^0\pi^-$ (right hand side).

mass. In Fig. 22 one example for differential results is shown. Plotted are the leading A_1 and A_2 coefficients for the proton target as function of W for different bins of the cm polar angle $\Theta_{\pi\pi}^*$ of the pion-pion system (the cm polar angle of the recoil nucleon is $\Theta_N^* = 180^\circ - \Theta_{\pi\pi}^*$). The asymmetries must vanish for $\Theta_N^* = 0^\circ, 180^\circ$ because in this cases the recoil nucleon and the incident photon are colinear so that no reaction plane is defined. The results for the asymmetries are of course statistically dominated by the values around $\Theta_{\pi\pi}^* = 90^\circ$ (which is one of the reasons why the detection efficiencies cancel even in the ratio of the integrated asymmetries). Also for the differential results for proton and neutron the A_1 coefficients seem to be approximately related by Eq. 5. A prominent feature of all three asymmetries is the zero crossing of the A_1 coefficients at $W=1525$ MeV, which is not reproduced by the model (see. Figs. 18,19,20).

In the following we compare the measured asymmetries to the results from reaction models. The Valencia model [33,36] reproduced many features of this reaction in the second resonance region (total cross sections, invariant-mass distributions, split into $\sigma_{1/2}$ and $\sigma_{3/2}$ components of the cross section) reasonably well but failed for the beam-helicity asymmetry in the second resonance region [35]. Predictions for higher incident photon energies or for the neutron target are not available from this model. Predictions from the Bonn-Gatchina (BnGn) model, which described the $p\pi^0\pi^0$ data quite well [15], are also not yet available for this isospin channel. However, such analyses

are now under way. The Bonn-Gatchina group has recently extended their coupled channel analysis [51] to the neutron target [52] and is currently including further reaction channels into the model.

The Two-Pion MAID model [22] was in reasonable agreement with the beam-helicity asymmetries for neutral pion pairs [15,35] in the second resonance region, although it reproduced total cross sections at low incident photon energies [14] not so good. However, it also failed for the asymmetries of the mix-charged pairs [35] in that energy region. Currently this model is the only one that made predictions up to higher incident photon energies and for reactions off the proton and off the neutron, which are compared in the figures to the measured asymmetries.

We discuss first the three ‘charge-ordered’ asymmetries I_{1c}° , I_{2c}° , I_{3c}° . The result is somewhat surprising. The results from the model are at least in reasonable agreement with the experimental findings for final-state invariant masses above 1550 MeV (cf Figs. 16,17). However, as already discussed in [35] for I_{1c}° , they disagree with the data and are out-of-phase for smaller W in the second resonance region. One would expect that at these low energies, with only a small set of well-known nucleon resonances contributing, the model should perform more reliably than at higher energies, but the contrary is the case.

The situation for the ‘invariant-mass ordered’ asymmetries I_{1m}° (Figs. 15,21) is even worse. Predictions for this observable fail in the second and in the third resonance region. Only at intermediate W (1550 - 1650 MeV)

they are similar to the data, which indicates that also for large W the dynamics of the reaction mechanism is not completely understood.

6 Summary and conclusions

Precise results have been measured for the first time for several types of beam-helicity asymmetries in the production of $\pi^0\pi^{+/-}$ pairs off free protons from a hydrogen target and off quasi-free protons and neutrons from a deuterium target with a circularly polarized photon beam. Together with the results published in [15] for the $\gamma N \rightarrow N\pi^0\pi^0$ reaction and for $\gamma p \rightarrow p\pi^+\pi^-$ [34] such asymmetries are now available for five different isospin channels of double pion production.

The asymmetries are sizable and the results for free and quasi-free protons are in excellent agreement when the kinematics of the quasi-free reaction are completely reconstructed. This justifies the interpretation of the quasi-free data for photoproduction off neutrons as a close approximation of free neutron data.

At present only one reaction model, the Pion-MAID model [22], has made predictions for both reactions over the full energy range, but further model analyses are under way. For the comparison between data and model results one can roughly distinguish three different ranges of final state invariant mass W . These are the second resonance peak ($W \leq 1540$ MeV), the third resonance peak ($W \geq 1660$ MeV), and the region in between.

The analysis of the $\gamma N \rightarrow N\pi^0\pi^\pm$ reaction has a difficult history for the second resonance region [1]. Early measurements of total cross sections and invariant mass distributions did not agree with any model predictions. Agreement became better when significant contributions from the ρ -meson were introduced into the models, but the previous experimental results for the asymmetry I_{1c}° for free protons [35] did again not agree with model predictions. The present results show that for all four considered asymmetries in this energy range the experimental data for proton and neutron targets are very similar but the model predictions are in all cases completely out of phase with them. Similar discrepancies have been reported in [35] for the Valencia model [36]. This is a strong indication that the reaction mechanisms for the second resonance region are simply not yet understood. The situation is different for the photoproduction of neutral pion pairs [35,15]. In that case good agreement of the asymmetry I_{1m}° (other asymmetries are not available) with model predictions was found in the second resonance region for protons and neutrons. This suggests that the problems for the mixed-charge channel are not due to the contributions of sequential resonance decays (which contribute to the production of $\pi^0\pi^0$ and $\pi^0\pi^\pm$ according to the respective Clebsch-Gordan coefficients) but to contributions that are not present for the $N\pi^0\pi^0$ final state. These are in particular processes involving the ρ -meson or non-resonant terms in charged pion production (pion-pole terms, Δ -Kroll-Ruderman etc.).

The poor agreement between experimental data and results from reaction models for asymmetries involving production of pion pairs with at least one charged pion [34,35] raised the question whether these observables are well suited for the study of nucleon resonances or are possibly too sensitive to interference terms with small background contributions. But the picture that emerges from the present results is somewhat different. The asymmetries predicted for the intermediate energy range ($1540 \text{ MeV} \leq W \leq 1660 \text{ MeV}$) are in much better agreement with the measurements. Here, it does not look like a severe discrepancy but more like the necessity for some fine tuning of the model. Also in the third resonance region the ‘charged-ordered’ asymmetries are already in reasonable agreement with measurements, although the ‘mass-ordered’ asymmetry is not yet reproduced. However, one should note that all asymmetries have been predicted by a reaction model that was not fitted to data but used only input for nucleon resonance parameters from the Particle Data Group. When more observables become available for the double-pion photoproduction those parameters could of course be fitted to the data.

The main conclusion is therefore that a specific problem for the production of ‘mixed-charge’ pairs in the second resonance peak persists, while for higher final-state invariant masses the model predictions are already reasonable when one considers that up to now they could only be tested versus differential cross section data and that a ‘complete experiment’ for double-pion production would require the measurement of at least 15 observables. Analyses of the data in the framework of further reaction models are necessary and under way and further observables (invariant mass distributions of pion-pion and pion-nucleon pairs, target asymmetry T , and double polarization asymmetries E and F) have already been measured and are under analysis.

Acknowledgments

We wish to acknowledge the outstanding support of the accelerator group and operators of MAMI. This work was supported by Schweizerischer Nationalfonds, Deutsche Forschungsgemeinschaft (SFB 443, SFB/TR 16), DFG-RFBR (Grant No. 05-02-04014), UK Science and Technology Facilities Council, STFC, European Community-Research Infrastructure Activity (FP6), the US DOE, US NSF and NSERC (Canada).

References

1. B. Krusche and S. Schadmam, Prog. Part. Nucl. Phys. **51**, 399 (2003).
2. Ch. Chen et al., Few Body Syst. **53**, 293 (2012).
3. G. Eichmann Prog. Part. Nucl. Phys. **67**, 234 (2012).
4. I.G.Aznauryan et al., Int. J. Mod. Phys. E **22**, 1330 (2013).
5. R.G. Edwards et al., Phys. Rev. D **84**, 074508 (2011).
6. F. Härter et al., Phys. Lett. B **401**, 229 (1997).
7. A. Zabrodin et al., Phys. Rev. C **55**, R1617 (1997).
8. A. Zabrodin et al., Phys. Rev. C **60**, 055201 (1999).
9. M. Wolf et al., Eur. Phys. J. A **9**, 5 (2000).

10. V. Kleber et al., Eur. Phys. J. A **9**, 1 (2000).
11. M. Kotulla et al., Phys. Lett. B **578**, 63 (2004).
12. A.V. Sarantsev et al., Phys. Lett. B **659**, 94 (2008).
13. U. Thoma et al., Phys. Lett. B **659**, 87 (2008).
14. F. Zehr et al., Eur. Phys. J. A **48**, 98 (2012).
15. M. Oberle et al., Phys. Lett. B **721**, 237 (2013).
16. V. Kashevarov et al., Phys. Rev. C **85**, 064610 (2012).
17. J. Ajaka et al., Phys. Rev. Lett. **100**, 052003 (2008).
18. I. Horn et al., Phys. Rev. Lett. **101**, 202002 (2008).
19. I. Horn et al., Eur. Phys. J. A **38**, 173 (2008).
20. V. Kashevarov et al., Eur. Phys. J. A **42**, 141 (2009).
21. V. Kashevarov et al., Phys. Lett. B **693**, 551 (2010).
22. A. Fix and H. Ahrenhövel, Eur. Phys. J. A **25** 115 (2005); interactive version available at <http://wwwkph.kph.uni-mainz.de/MAID//maid.html>
23. M. Ripani et al., Phys. Rev. Lett. **91**, 022002 (2003).
24. G.V. Fedotov et al., Phys. Rev. C **79**, 015204 (2009).
25. V.I. Mokeev et al., Phys. Rev. C **80**, 045212 (2009).
26. V.I. Mokeev et al., Phys. Rev. C **86**, 035203 (2012).
27. A. Braghieri et al., Phys. Lett. B **363**, 46 (1995).
28. W. Langgärtner et al., Phys. Rev. Lett. **87**, 052001 (2001).
29. K. Ochi et al., Phys. Rev. C **56**, 1472 (1997).
30. J.C. Nacher et al., Nucl. Phys. A **695**, 295 (2001).
31. W. Roberts and T. Oed, Phys. Rev. C **71**, 055201 (2005).
32. J. Ahrens et al., Phys. Lett. B **551**, 49 (2003).
33. J.C. Nacher and E. Oset, Nucl. Phys. A **697**, 372 (2002).
34. S. Strauch et al., Phys. Rev. Lett. **95**, 162003 (2005).
35. D. Krambrich et al., Phys. Rev. Lett. **103**, 052002 (2009).
36. L. Roca, Nucl. Phys. A **748**, 192 (2005).
37. B. Krusche, Eur. Phys. J. Special Topics **198**, 199 (2011).
38. I. Jaegle et al., Eur. Phys. J. A **47**, 89 (2011).
39. H. Herminghaus et al., IEEE Trans. on Nucl. Science. **30**, 3274 (1983).
40. K.-H. Kaiser et al., Nucl. Instr. Meth. A **593**, 159 (2008).
41. I. Anthony et al., Nucl. Instr. Meth. A **301**, 230 (1991).
42. S.J. Hall, G.J. Miller, R. Beck, P.Jennewein, Nucl. Inst.Meth. A **368**, 698 (1996).
43. J.C. McGeorge et al., Eur. Phys. J. A **37**, 129 (2008).
44. H. Olsen and L.C. Maximon, Phys. Rev. **114**, 887 (1959).
45. A. Starostin et al., Phys. Rev. C **64**, 055205 (2001).
46. R. Novotny, IEEE Trans. on Nucl. Science **38**, 379 (1991).
47. A.R. Gabler et al., Nucl. Instr. Meth. A **346**, 168 (1994).
48. D. Watts, in *Calorimetry in Particle Physics, Proceedings of the 11th International Conference, Perugia, Italy 2004*, edited by C. Cecchi, P. Cenci, P. Lubrano, and M. Pepe (World Scientific, Singapore, 2005), p. 560
49. S. Schumann et al., Eur. Phys. J. A **43** 269 (2010).
50. S. Agostinelli et al., Nucl. Instr. Meth. A **506** 250 (2003).
51. A.V. Anisovich et al., Eur. Phys. J. A **44**, 203 (2010).
52. A.V. Anisovich et al., Eur. Phys. J. A **49**, 67 (2013).
53. V.E. Tarasov et al., Phys. Rev. C **84**, 035203 (2011).
54. W. Chen et al., Phys. Rev. C **86**, 015206 (2012).
55. M. Dieterle et al., submitted to Phys. Rev. Lett (2014)
56. I. Jaegle et al., Phys. Rev. Lett. **100**, 252002 (2008).
57. I. Jaegle et al., Eur. Phys. J. A **47**, 11 (2011).
58. D. Werthmüller et al., Phys. Rev. Lett. **111**, 232001 (2013).
59. L. Witthauer et al., Eur. Phys. J. A **49**, 154 (2013).

